Reversible Pressure-Magnetic Modulation in a Tetrathiafulvalene-Based Dyad Piezochromic Dysprosium Single-Molecule Magnet

Fabrice Pointillart,*[a] Jessica Flores Gonzalez,[a] Haiet Douib,[a] Vincent Montigaud,[a] Charles J. McMonagle,[b] Boris Le Guennic,*[a] Olivier Cador,[a] Dawid Pinkowicz*[c] and Michael R. Probert[b]

[a] Univ Rennes, CNRS, ISCR (Institut des Sciences Chimiques de Rennes) - UMR 6226, F-35000 Rennes, France

[b] Chemistry, School of Natural and Environmental Sciences, Newcastle University, Newcastle upon Tyne, NE1 7RU, United Kingdom

[c] Faculty of Chemistry, Jagiellonian University, Gronostajowa 2, 30-387 Kraków, Poland

ABSTRACT: The extreme sensitivity of trivalent lanthanide ions to crystal field variations led to the emergence of single-molecule magnetic switching under various stimuli. The use of pressure as an external stimulus instead of classic light irradiation, oxidation or any chemical reactions allows a fine tuning of the magnetic modulation. Here the well-known pure isotopically enriched $[^{162}Dy(tta)_3(\textbf{L})]\cdot C_6H_{14}$ ($^{162}\textbf{Dy}$) Single-Molecule Magnet (SMM) (tta^- = 2-2-thenoyltrifluoroacetonate and $\textbf{L}$ = 4,5-bis(propylthio)-tetrathiafulvalene-2-(2-pyridyl)benzimidazole-methyl-2-pyridine) was experimentally investigated by single-crystal diffraction and squid magnetometry under high applied pressures. Both reversible piezochromic properties and pressure modulation of the SMM behavior were demonstrated and supported by ab initio calculations. The magnetic study of the diluted sample $[^{162}Dy_{0.05}Y_{0.95}(tta)_3(\textbf{L})]\cdot C_6H_{14}$ ($^{162}\textbf{Dy@Y}$) indicated that variations in the electronic structure have both intra- and inter-molecular origins. Quantitative magnetic interpretation concludes to a deterioration of the Orbach process for the benefit of both Raman and QTM mechanisms under applied pressure.

INTRODUCTION

In the context of systems suitable for potential applications in high density data storage, the discovery of the Single-Molecule Magnet (SMM) behavior for a cluster of twelve manganese ions[1-2] paved an exciting research way in the molecular magnetism field. The difficulties to push the boundaries of the performances due to the equilibrium between magnetic anisotropy and spin values associated to the discovery of the first mononuclear lanthanide SMM,[3] this led to a virtual monopoly for lanthanide chemistry in the design of high performance SMMs.[4-8] The use of computational approaches to better understand the needed prerequisites helped to optimize such systems.[9-10] Thus the strong uniaxial magnetic anisotropy observed in organometallic lanthanide complexes allowed the observation of a high blocking temperature, up to 80 K.[11-14] Such molecular systems which display magnetic bistability could become good candidates to applications such as quantum computing[15] and spintronics.[16] With the aim to extend the range of potential applications dedicated to SMMs, the reversible modification of the magnetic behavior by applying external stimuli opens the possibility to design switches and sensors.[17] The switching of SMM behavior in lanthanide molecular systems is usually reached using i) chemical agents for redox reaction[18-21] and pH variation,[22-23] ii) selected solvents,[24-27] iii) light irradiation[28-31] or iv) a combination of several stimuli.[32-33] As recently reviewed,[34] lanthanides are ideal elements for the design of molecular switches since they are extremely sensitive to crystal field effects, in other words, to any structural changes in the first coordination sphere or even farther in the crystal packing. Obviously, the listed-above stimuli induced chemical modifications of the target system such as ligand or/and metal-centered oxidation state, isomerization, protonation, modification of the coordination number... leading, from a chemical point of view, to different starting and final systems. Thus, an applied pressure as external stimulus appears as a promising alternative to finely tune the SMM behavior. The few examples of such studies have been carried out mainly on the pioneering Mn_{12} system,[35-37] as well as on other manganese-based SMMs.[38-41] To the best of our knowledge, only two examples of lanthanide complexes studied under applied pressure have been reported to date. Nevertheless, in both examples the applied pressure induced the loss of crystallinity due to the release of solvent molecules[42] or phase transition.[43]

The mononuclear complex of formula $[Dy(tta)_3(\textbf{L})]\cdot C_6H_{14}$ (tta^- = 2-2-thenoyltrifluoroacetonate and $\textbf{L}$ = 4,5-bis(propylthio)-tetrathiafulvalene-2-(2-pyridyl)benzimidazole-methyl-2-pyridine) was selected from our library of compounds for high pressure studies because its magnetic properties are experimentally and computationally well-known,[44] magnetic dilutions and isotopic enrichment studies were performed[45-47] as well as spectroelectrochemistry investigations.[48] Moreover the nuclear spin free $^{162}Dy(III)$ (I = 0) ion was chosen to cancel the hyperfine coupling and to diminish the under-barrier magnetic relaxation mechanisms. Therefore, here we present the high-pressure single crystal X-ray diffraction study and magnetic investigations of $[^{162}Dy(tta)_3(\textbf{L})]\cdot C_6H_{14}$ ($^{162}\textbf{Dy}$). The magnetic measurements are completed by those of the diluted analogue $[^{162}Dy_{0.05}Y_{0.95}(tta)_3(\textbf{L})]\cdot C_6H_{14}$ ($^{162}\textbf{Dy@Y}$). Finally, periodic Density Functional Theory (DFT) and multireference wavefunction theory calculations were conducted to rationalize both structural and magnetic results.

RESULTS AND DISCUSSION

Structural Characterization. Both [162]Dy and [162]Dy@Y compounds have been previously synthetized and characterized by IR and UV-visible spectroscopies, elemental analyses, and Scanning Electron Microscopy (SEM).[44,47] The structure for the natural element (**Dy**)[44], at ambient temperature, and for [162]Dy and [162]Dy@Y[47] at 150 K have previously been determined by single crystal X-ray diffraction.
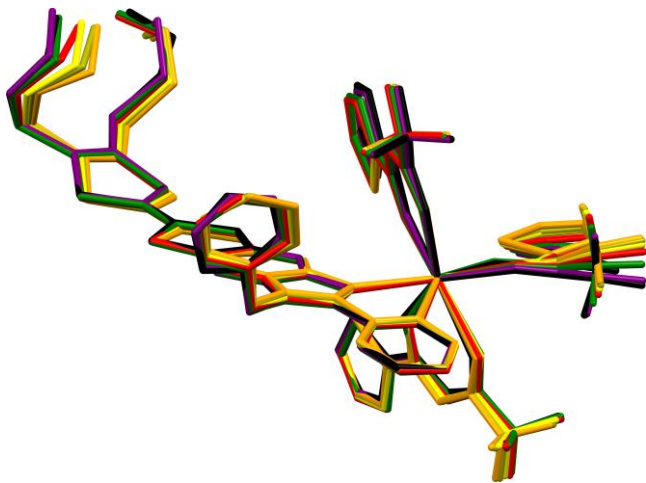

Figure 1. X-ray structure of [162]Dy recorded in the pressure range 0-2.43 GPa: P = 0 GPa (black), P = 0.22 GPa (purple), P = 0.46 GPa (green), P = 1.17 GPa (red), P = 1.63 GPa (yellow), P= 2.10 GPa (yellowish) and P = 2.43 GPa (orange).

Ambient Pressure Crystal Structure. The ambient pressure X-ray structure of **Dy** at room temperature is quickly described below. It crystallizes in the P-1 (N°2) triclinic space group. The X-ray structure revealed the formation of a mononuclear complex for which the Dy(III) center is linked to three tta⁻ anions and one **L** ligand through the (2-pyridyl)benzoimidazolyl (bzip) fragment (Figure 1) while a *n*-hexane solvent molecule co-crystallizes with the complex. The ligand arrangement of the resulting N_2O_6 coordination sphere led to a square antiprism with a deviation from the ideal D_{4d} symmetry of 0.54 (from SHAPE analysis).[49] The average Dy-N and Dy-O bond lengths are 2.530(5) Å and 2.333(4) Å, respectively. The location of the thiophene groups containing S31, S41, and S51 are noted in Figure S1. The neutral form of the TTF-based ligand is confirmed by the C=C central bond length of 1.347(9) Å and boat conformation. The formation of "head-to-tail" dimers of complexes are identified in the crystal packing (Figure S2) thanks to π-π interactions between the donor (TTF fragment) and acceptor (bzip) parts of the **L** dyad.

High-Pressure Crystal Structure. The structure of [162]Dy was determined at high-pressure using single crystal X-ray diffraction in the pressure range of 0.22 to 2.43 GPa (Table S1). On increasing pressure, the compression of the unit cell was found to be highly anisotropic with the *a* and *b* axes compressing more than the *c* axis (Figure S3a) with 10.3, 9.1 and 4.8 % of reduction, respectively. The angles are not strongly modified. The volume of the cell decreases from 3280 Å³ at ambient pressure to 2640 Å³ at 2.43 GPa. To give more insights on the pressure effect on the crystal structure, a series of periodic DFT optimizations were performed at selected isostatic pressures ranging from 0 to 2.5 GPa (see Computational Details in the Experimental part). To investigate potential effects of higher pressures

on the structure, two additional points were added in the study (3 and 5 GPa). The trend of the calculated cell parameters agrees with the experimental one within the 0-2.5 GPa window (Figures S3a-c, Table S2) and validates the deformation in the [110] plane. One could identify a slight deviation between experimental and calculated trend for the γ angle at P > 1.5 GPa. Even though the effects upon the unit cell angles appear very limited, the increase of the applied pressure reduces *b* and *c* parameters reaching a minimum value at 3 GPa while *a* parameter continues to decrease. The calculations show that at 2.5 GPa, the structure almost reaches the maximal compression of the *bc* plane leaving only one degree of freedom for the dimers to shift in the cell along the *a*-axis. Further increasing the external pressure, up to 5 GPa, induces the reduction of *a* parameter down to 13.2 Å while *b* and *c* converge.

The effects of increasing pressure can be seen with intramolecular distortions. The first coordination sphere of the Dy is particularly of interest. There is a reduction in the average Dy-O distances under increasing applied pressure. This average reduction was expected however the individual Dy-O are far from homogeneous. Under 2.43 GPa, Dy-O1, Dy-O4, and Dy-O6 are strongly affected respectively compressing by 2.4, 3.0, and 3.7 % of their initial length (ambient pressure). Dy-O2 (0.5 %) and Dy-O3 (0.3 %) weakly compressed while Dy-O5 is found to elongate (-1.9 %) (Figure S4, Table S3). For each ancillary ligand (tta⁻ anions), one Dy-O bond length is compressed (Dy-O1, Dy-O4, and Dy-O6) while the second one is almost not affected (Dy-O2 and Dy-O3) or elongated (Dy-O5) under pressure. A similar trend is observed for the Dy-N distances with a strong (4.2 %) and weak (1.1 %) compression for Dy-N1 and Dy-N2, respectively (Figures 2 and S5, Table S3).
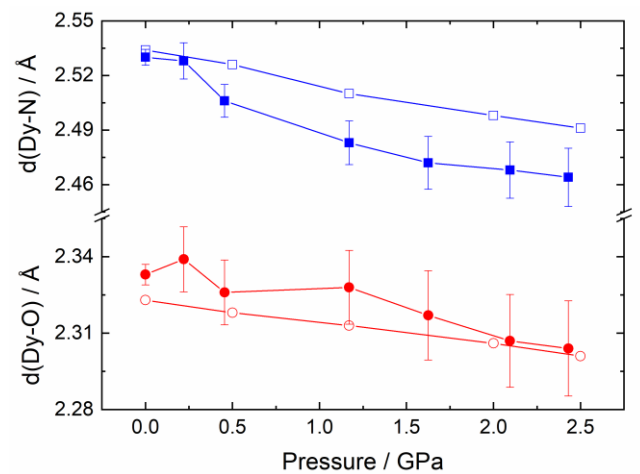

Figure 2. Experimental (full symbols) and calculated (empty symbols) variations of the average Dy-O (red) and Dy-N (blue) distances with pressure.

The compression trends are also observed for the Dy-O and Dy-N distances in the DFT optimized structures (Table S4). The pressure induces an increase of the Dy-X (X = O and N) bond length distribution (Figures S3 and S4) which is illustrated by the increase of the CShM(D_{4d}) coefficient (Figure S6) determined by the SHAPE analysis.[49] Indeed the Dy-O and Dy-N distances range respectively from 2.311 to 2.347 Å and 2.496 to 2.564 Å at P = 0 GPa while at 2.43 GPa they range from 2.240 to 2.380 Å and 2.390 to 2.536 Å. The CShM(D_{4d}) increases from 0.54 to 0.65 (Figure S6).
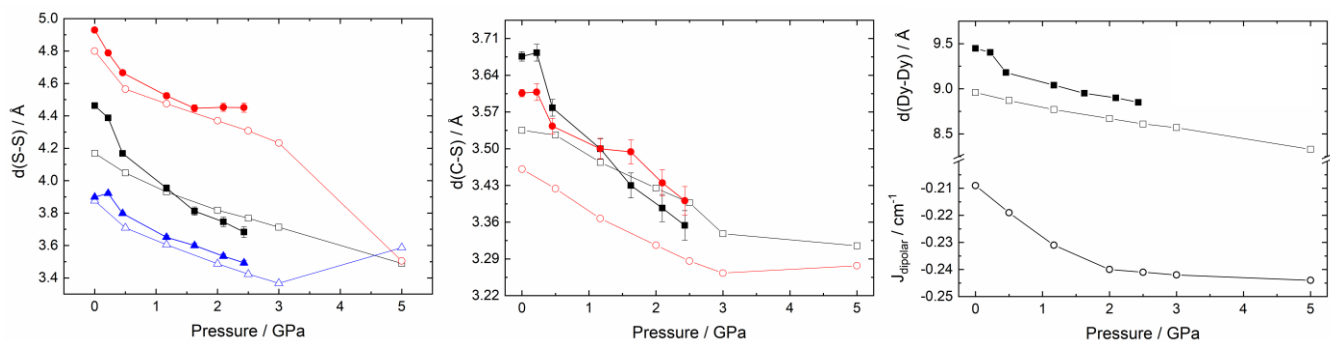
Figure 3. Pressure variations of the experimental (full symbols) and calculated (empty symbols) intramolecular distances S31···S51 (blue triangles), S31···S41 (black squares) and S41···S51 (red circles) (a), intermolecular distances C5···S4 (black squares) and C14···S2 (red circles) (b) and Dy···Dy (black squares) (c). (c) Pressure variation of the calculated antiferromagnetic dipolar interaction $J_{dipolar}$ (open black circles).

At ambient pressure, the three thiophene groups formed only one short S31···S51 contact (3.899 Å) (Figures 3a and S5). All the S···S intramolecular distances decrease with pressure, reaching two short S31···S51 (3.493 Å) and S31···S41 (3.683 Å) contacts (black squares, Figures 3a and S7) at the highest experimental pressure (2.43 GPa). The calculations show that at 5 GPa, the three sulfur atoms form a triangle of short S31···S51 (3.587 Å), S31···S41 (3.489 Å) and S41···S51 (3.505 Å) contacts (Figures 3a and S7). These intramolecular S···S contacts may be one of the parameters which drives the deformation of the coordination sphere around the Dy(III) center. From an intermolecular point of view, the compression along the *b* axis is visible through the π-π distance between the two **L** ligands composing a dimer. Thus the shortest intermolecular C···S distances decrease from 3.606 (0 GPa) to 3.354 Å (2.43 GPa). The calculations show that these distances can further decrease reaching their shortest distance at 3 GPa (Figures 3b and S8) as observed for the *b* parameter (Figure S3). Finally, Figure 3c illustrates the decrease of the intermolecular Dy···Dy distance (6.3 %) with pressure. Both computed pressure variations of the C···S and Dy···Dy intermolecular distances are in agreement with the experiment demonstrating the pertinence of the periodic DFT approach to determine the optimized structures under isostatic pressure.

Piezochromism. Single crystals of [162]**Dy** are orange and no change of color was observed when the crystals were ground or during the measurement of physical properties.[47] The color is attributed to the HOMO → LUMO intra-ligand charge transfer (ILCT) centered at 23200 cm^{-1} (430 nm) where the HOMO and LUMO are respectively centered on the TTF and bzip fragments.[44] Thus the color change can be connected to the energy of the ILCT excitation. It is also well-known that such energy can be modulated by oxidation of the TTF fragment[48] or by coordination of the electron withdrawing metal unit.[50] Figure S1 shows that a single crystal of [162]**Dy** changes of color from orange to purple when applying an external pressure from 0.22 GPa to 2.43 GPa. This piezochromic phenomena could be explained by pressure perturbation to the LUMO energy level of the related ILCT transition because of the shortening of the Dy-N1 bond length which increase the electrostatic effect of the Dy(tta)$_3$ coordination. Piezochromism is reversible since the single crystal recovers its initial color releasing the cell pressure (see video in SI).

Magnetism. The thermal dependence of the $\chi_M T$ at P = 0 GPa, 0.31 GPa, 1.17 GPa and back to 0 GPa are depicted in Figure S9.
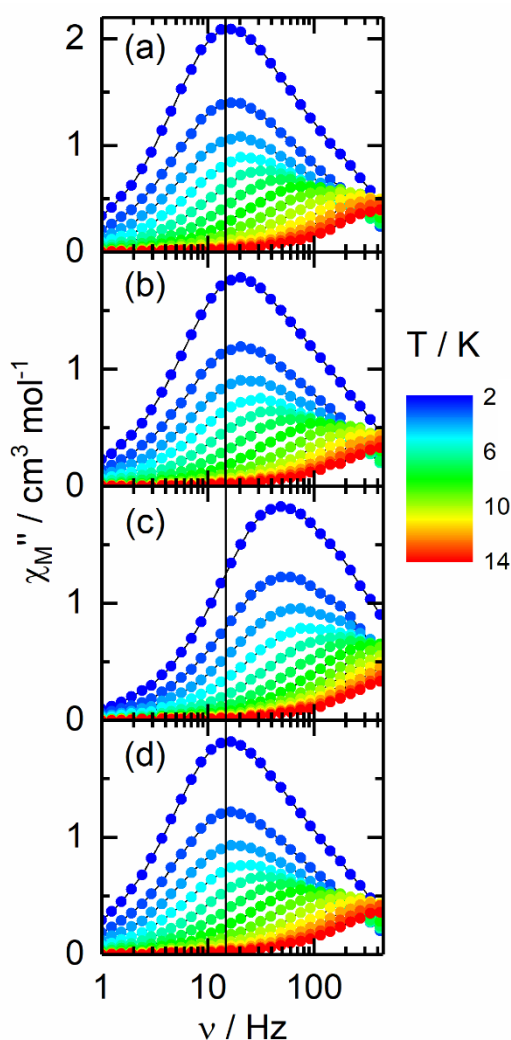

Figure 4. Frequency dependence of χ_M'' in the temperature range 2-14 K for [162]**Dy** under P = 0 GPa (a), P = 0.31 GPa (b), P = 1.17 GPa (c) and back to P = 0 GPa (d) in zero applied magnetic field. The full vertical line is guide to the eye only.

The measurements are limited to the 5-100 K temperature range due to the used setup. No significant effect of the pressure could

be observed on the $\chi_M T(T)$ curves on such temperature range. The frequency dependences of the magnetic susceptibility (χ_M) have been measured to determine the dynamic magnetic properties of [162]**Dy** at ambient pressure (0 GPa) and high pressure (0.31 and 1.17 GPa). It is worth noting that the dynamic magnetic properties of [162]**Dy** at ambient pressure are already well-known[47] but the measurements were repeated using the same squid magnetometer and set up as the high-pressure magnetic measurements. At P = 0 GPa, [162]**Dy** displays frequency dependence of the magnetic susceptibility (Figures 4a and S10a), the appearance of an out-of-phase component (χ_M") in zero applied magnetic field is sign of slow magnetic relaxation. At 2 K, the maximum on the χ_M" vs. ν curve (where ν is the frequency of the oscillating field) is centered at 15 Hz (Figure 4a) in agreement with the published frequency value[46] highlighting that the pressure cell has no significant influence.
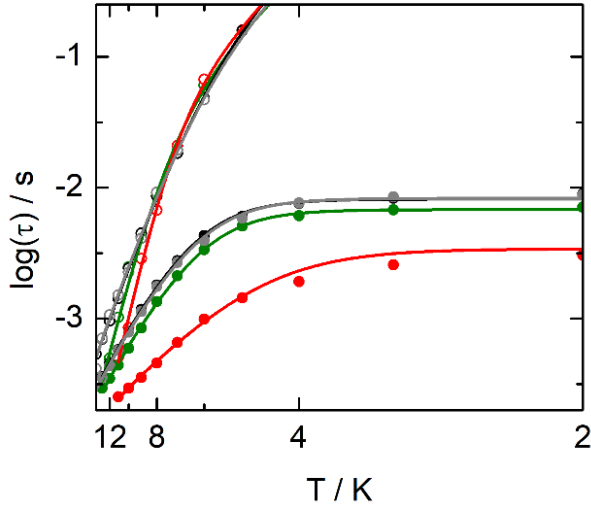

Figure 5. Arrhenius plots of the relaxation time in zero applied magnetic field (full symbols) and at 1000 Oe (empty symbols) for [162]**Dy** at P = 0 GPa (black), P = 0.31 GPa (green), P = 1.17 GPa (red) and back to P = 0 GPa (gray). Full lines are the best-fitted curves (see text). The relaxation time at 5 K under 1000 Oe was manually extracted.

Increasing the applied pressure, the slow magnetic relaxation is preserved but shifts to higher frequencies with maxima at 2 K centered at 20 Hz for 0.31 GPa (Figure 4b) and 50 Hz (Figure 4c) for 1.17 GPa. The effect of the pressure is reversible since the release of the pressure allowed the recovery of the initial ac data (Figure 4d) and that is in line with the reversible piezochromic effect. The relaxation time τ was extracted at each temperature and applied pressure using an extended Debye model (details in SI, Table S5) to fit simultaneously the frequency dependence of χ_M'' and of the in-phase susceptibility χ_M' (Figure S11). Figures S12-S15 show the normalized Cole-Cole plots in the temperature range of 2 to 14 K. Whatever the pressure, the resulting plots adopt a semi-circle shape giving a narrow distribution of the relaxation times ($0.01<\alpha<0.15$) (Tables S5-S8). The relaxation time follows a combination of thermally dependent and thermally independent processes (Figure 5). Until the present work, the Arrhenius law of the [x]**Dy** (x = 161 to 164) systems in its natural and its isotopically enriched form was fitted using a combination of Orbach and QTM process and neglecting the Raman process[47] (equation 1):

$$\tau^{-1} = \underbrace{CT^n}_{Raman} + \underbrace{\tau_0^{-1} \exp\left(-\frac{\Delta}{kT}\right)}_{Orbach} + \underbrace{\tau_{TI}^{-1}}_{QTM} \qquad \text{Eq. 1}$$

Using such an approach, the best fits of the thermal dependence of the relaxation time in the pressure range of 0-1.17 GPa in zero applied magnetic field are shown in Figure S16 with the parameters in Table S9.

The ac magnetic properties were studied under an applied optimal magnetic field of 1000 Oe in the pressure range 0-1.17 GPa (Figures S17 and S18). The magnetic field cancels the fast magnetic relaxation through Quantum Tunneling of the Magnetization (QTM) and thus the maxima of the χ_M" are shifted to the lower frequencies. The same method than for zero magnetic field was used to extract the relaxation time τ at 1000 Oe (Tables S10-13). The distribution of the relaxation times increases ($0.01<\alpha<0.40$) due to the dc applied magnetic field (Figures S19-22). Under the 1000 Oe optimal field, the relaxation time follows thermally dependent processes with a deviation from the linearity at low temperature which has been attributed to the Raman contribution (Figure 5, equation 1). Thus, the thermal dependence of the relaxation time at P = 0 GPa and H = 1000 Oe was fitted using a combination of Orbach and Raman processes.

Table 1. Dynamic parameters of the different relaxation mechanisms for the [162]**Dy** in the pressure range of 0-1.17 GPa.

P / GPa	H / kOe	Δ / K	τ_o / s	C / K^{-n} s^{-1}	n	τ_{TI} / s
0	0	34.7(7)	3.2(3)×10^{-5}	0.0025(2)	4.76	0.0082
0	1	54(1)	1.6(2)×10^{-5}			-
0.31	0	34(1)	2.6(5)×10^{-5}	0.0032(2)	4.76	0.0068
0.31	1	82(4)	8(3)×10^{-5}			-
1.17	0	21(4)	4.4(8)×10^{-5}	0.0028(2)	4.76	0.0034
1.17	1	90(5)	1.5(7)×10^{-5}			-
Back to 0	0	34(1)	3.4(5)×10^{-5}	0.0029(6)	4.76	0.0083
Back to 0	1	55(3)	1.7(3)×10^{-5}			-

The best fit was obtained for an Orbach regime with $\Delta = 53(3)$ K, $\tau_0 = 1.7(8) \times 10^{-5}$ s and Raman regime $C = 2.4(2) \times 10^{-3}$ s^{-1} K^{-n}, $n = 4.76(56)$ between 5 and 14 K. The expected n value for Kramers ions should be 9,[51] but the presence of both acoustic and optical phonons could lead to lower values comprised between 2 and 7.[52-55] In order to prevent any over parametrization, all the next fits have been realized with fixed $n = 4.76$ and the QTM fixed to the values found using a combination of Orbach and QTM processes only (Table S9). The Raman process is considered field independent (equation 1)[56] for a given pressure but variable as a function of the applied pressure since such stimulus induced reorganization of the electronic distribution around the Dy(III) center and variation of the interaction between the complex and the matrix. Then, the thermal variation of the relaxation time at a specific pressure is simultaneously fitted for ^{162}Dy under 0 Oe and 1000 Oe with contribution of two effective Orbach processes, Raman shared parameters and zero-field only QTM. The best fits for P = 0 GPa (Figure S23), P = 0.31 GPa (Figure S24), 1.17 GPa (Figure S25) and back to P = 0 GPa (Figure S26) are given in the Table 1 and displayed in Figure 5. From the data of Table 1, one could remark that i) the energy barrier values increased under applied magnetic field for a given pressure due to the reduction of ground-state QTM,[57] ii) in zero magnetic field, the increase of applied pressure led to a decrease of the fitted energy barrier and an increase of the QTM which could be related to the distortion of the coordination sphere around the Dy(III) center (Figure S6) and iii) the pressure effect on the dynamic magnetic properties is reversible. Nevertheless, no significant variation of the Raman process (CT^n) was observed (Table 1). This could be due to the available data limited to the experimental temperature range of 5-12 K because the system displays too slow magnetic relaxation at lower temperature for our setup. Thus, lower temperature dc measurements could give more insights on this point.

The classical butterfly shape hysteresis loops for ^{162}Dy was measured at 2 K and P = 0 GPa then compared to those under applied pressure (Figure 6). While all the hysteresis loops remain close at zero field due to the QTM, significant differences are observed in field.
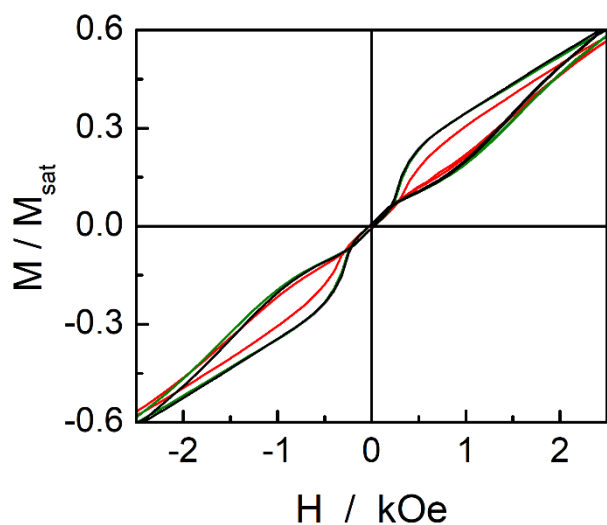

Figure 6. Magnetic hysteresis loops at 2 K and at a sweep rate of 16 Oe s^{-1} for ^{162}Dy at 0 GPa (black), 0.31 GPa (green) and 1.17 GPa (red).

Application of high-pressure tends to close the hysteresis loop in field ($\delta = 650$ Oe at H = 1000 Oe for P = 0 GPa and ($\delta = 400$ Oe at H = 1000 Oe for P = 1.17 GPa) (Figure S27) in agreement with the increase of the under energy barrier mechanisms (QTM and Raman). The previous magnetic investigation in frozen solution of **Dy**[43] and for diluted ^{162}**Dy**[47] undoubtedly demonstrated the presence of significant intermolecular dipolar interactions playing a drastic role in the magnetic behavior. Thus, to discriminate between an intra- and/or inter-molecular origin of the magnetic modulation under applied pressure, the magnetic study was carried out for the diluted ^{162}**Dy@Y** compound. The constraints due to the small volume of the setup and the weak magnetic response of ^{162}**Dy@Y** limited the magnetic study to the dc investigation. The butterfly shape hysteresis loops is also observed for ^{162}**Dy@Y** at 2 K and P = 0 GPa (Figure S28). A magnetic memory is observed at smaller applied magnetic field for ^{162}**Dy@Y** than for ^{162}**Dy** due to the decrease of QTM by magnetic dilution.
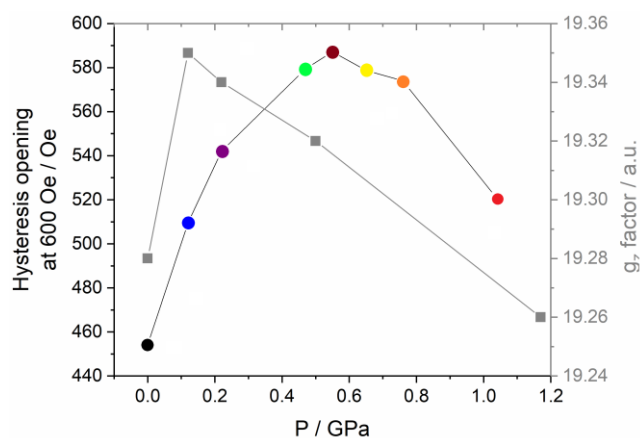

Figure 7. Hysteresis loop opening at H = 600 Oe and g_z factor values (gray full squares) in the pressure range of 0-1.04 GPa. Full lines are guides to the eye only.

The variation of the hysteresis opening is not homogenous in increasing the applied pressure. Indeed, the opening at 600 Oe first increases from $\delta = 450$ Oe at 0 GPa to $\delta = 590$ Oe at 0.55 GPa and then decreases to $\delta = 520$ Oe at 1.04 GPa (Figure 7). The variation of the hysteresis loop width of ^{162}**Dy@Y** is mainly representative of the intramolecular structural modification induced by the pressure. The magnetic modulation at a given applied field and the butterfly hysteresis shape could not be attributed to QTM since both hyperfine and dipolar interactions have been cancelled and might be due to the Raman process. From the DC magnetic investigations of ^{162}**Dy** and ^{162}**Dy@Y**, it appeared that the magnetic modulation under applied pressure are different leading to the involvement of both intra- and inter-molecular origins. It can be anticipated that wavefunction theory calculations could rationalize this magnetic behavior.

***Ab Initio* Calculations**. SA-CASSCF/RASSI-SO calculations were performed to propose a quantitative interpretation of the magnetic data. Such wavefunction calculations were carried out from the crystal structure of **Dy** at room temperature. In order to go one step forward compared to the calculations previously performed by some of us using an isolated complex ("gas phase"),[44] the structural model was optimized taking into account the neighboring complexes ("solid state") using periodic DFT calculations (Figure S29).

Table 2. Energy gap between the ground state (GS) and first excited state (ΔE) of the $^6H_{15/2}$ multiplet with composition of GS and g factor values at selected applied pressure.

P/GPa	g_x	g_y	g_z	GS	ΔE (cm^{-1})
0	0.02	0.03	19.28	90.6% ± 15/2	98.8
0.12	0.02	0.03	19.35	92.0% ± 15/2	103.0
0.22	0.02	0.03	19.34	91.0% ± 15/2	100.0
0.5	0.02	0.03	19.32	91.1% ± 15/2	96.6
1.17	0.04	0.06	19.26	90.4% ± 15/2	80.0
2	0.06	0.12	19.15	89.0% ± 15/2	63.2
2.5	0.10	0.23	18.99	87.9% ± 15/2	49.3
3	0.13	0.37	18.87	87.2% ± 15/2	40.2
5	0.05	0.31	18.94	87.1% ± 15/2	48.2

Based on the latter optimized structure, the ground state doublet (GS) for the single ion at P = 0 GPa has a slightly less Ising character (g_x = 0.02, g_y = 0.03 and g_z = 19.28, Table 2) than the GS obtained with the isolated complex (g_x = 0.00, g_y = 0.00 and g_z = 19.50, Table S14). The ground state doublet is mainly composed of M_J = ±15/2 (91%) and the orientation of the main anisotropy axis is calculated perpendicular to the plane involving the bzip fragment as expected for an oblate Dy(III) ion in a N_2O_6 coordination sphere (Figure S30).[57-62] The energy gap between the GS and the first excited state decreases from 125.7 cm^{-1} to 98.8 cm^{-1} (Figure S29 and Table S14). The calculated energy barrier of 98.8 cm^{-1} is higher than the effective energy barrier determined from the high temperature region of the Arrhenius plot at 0 Oe (23.6(2) cm^{-1}) and 1000 Oe (50.3(7) cm^{-1}) supporting the presence of significant under barrier magnetic relaxation mechanisms such as QTM and Raman. Calculations show that by applying weak pressure (P < 0.5 GPa), the uniaxial character of the GS magnetic anisotropy is enhanced (Table 2) while for higher pressure values, the transversal components of the g factor increase leading to more efficient QTM (Tables S15-S23). This trend perfectly agreed with what was observed with the hysteresis loop of ^{162}**Dy@Y**. One more important parameter is the decrease of the energy barrier for applied pressures P > 0.5 GPa as experimentally observed (Table 1). The matrix elements of the transition magnetic moments have been computed and depicted in Figure S31 in order to give more insights into the relaxation mechanisms. Thus the increase of applied pressure induced a decrease of the spin-phonon Orbach process (1.57 for 0 GPa to 0.90 for 2.0 GPa) in favor to both under barrier Raman (0.11 for 0 GPa to 0.57 for 3.0 GPa) and (0.02 for 0 GPa to 0.08 for 3.0 GPa) QTM processes (Figure S29). The hysteresis loops of both ^{162}**Dy** and ^{162}**Dy@Y** compounds suggested a significant role of the intermolecular interaction (J_{dip}), the latter were computed and evaluated to J_{dip} = -0.209 cm^{-1} at P = 0 GPa. Increasing the pressure, the absolute J_{dip} value increases to 0.244 cm^{-1} (Figure 3c) in agreement with the shortening of the intermolecular Dy···Dy distances (Figure 3c) and tends to reinforce the QTM.

CONCLUSIONS

In conclusion, this work demonstrated the possibility to reversibly modulate the SMM behavior of a mononuclear complex of Dy(III) applying pressure. The stimulus induced structural distortions at the molecular level at the origin of the change in the electronic properties. The combined magnetic investigations of ^{162}**Dy** and ^{162}**Dy@Y** under applied pressure demonstrated that the degradation of the SMM performances might be due to the decrease of the Orbach contribution in favor of the under-barrier Raman and QTM contributions. The pressure-magnetic modulation is doubtless due to both intra- (distortion of the coordination sphere around the metal center) and inter-molecular (dipolar interactions and interaction with the matrix) origins. This work reports a combination of reversible piezochromism and pressure-magnetic modulation of the SMM behavior. The ^{162}**Dy** compound enriches the family of multiple properties SMM and could open the route to the design of optical and magnetic molecular sensors.

EXPERIMENTAL PART

Materials and Methods. The compounds [^{162}Dy(tta)$_3$(**L**)]·C$_6$H$_{14}$ (^{162}**Dy**) and its diluted analogue [^{162}Dy$_{0.05}$Y$_{0.95}$(tta)$_3$(**L**)]·C$_6$H$_{14}$ (^{162}**Dy@Y**) (tta$^-$ = 2-thenoyltrifluoroacetylacetonate anion and **L** = 4,5-bis(propylthio)-tetrathiafulvalene-2-(2-pyridyl)benzimidazole-methyl-2-pyridine) were synthesized following previously reported method.[47] All solvents were dried using standard procedures. The isotopically enriched ^{162}Dy$_2$O$_3$ oxides are commercially available from Eurisotop and Innovachem companies. All other reagents were purchased from Merck Co. Ltd and were used without further purification.

X-ray diffraction study. High-pressure experiments on ^{162}**Dy** were performed using a modified Merrill-Bassett diamond anvil cell (DAC). A single-crystal was loaded into a stainless-steel gasket with ruby in the DAC to measure the pressure The pressure was measured before and after data collection and an average used. Fluorinert FC-70 was used as a pressure transmitting medium. These data were collected at room temperature on a Bruker D8 Vantage at Newcastle University equipped with a Incoatec Ag IµsK α (λ = 0.56086 Å) source and Photon II detector. Data were collected, using 10 phi scans to maximize accessible coverage. Sample reflections were identified using the reciprocal lattice viewer within the Apex II program[63] for initial unit cell refinement. Data integration and global cell refinement were performed with the program SAINT[64] and data were corrected for absorption with the program SADABS.[65] The minimum transmission factor for the high-pressure structures is due to partial shadowing from the DAC gasket. Structural solutions and least-squares refinements were carried out using the Olex2[53] interface to the SHELX[66,67] suite of programs. Suitable structures were obtained for six pressures: 0.22 GPa, 0.46 GPa, 1.17 GPa, 1.63 GPa, 2.10 GPa and 2.43 GPa. Complete crystal structure results as CIF files including bond lengths, angles, and atomic coordinates are deposited as Supporting Information. They have been deposited in the Cambridge Structural Database for ^{162}**Dy** at P = 0.22 GPa, 0.46 GPa, 1.17 GPa, 1.63 GPa, 2.10 GPa and 2.43 GPa, respectively.

Magnetic measurements. Magnetic measurements under pressure were performed using Quantum Design MPMS3 SQUID magnetometer equipped with a 7 T magnet. Polycrystalline samples of 11.5 mg for ^{162}**Dy** and 11.4 mg for ^{162}**Dy@Y** were loaded into the CuBe piston-cylinder type high pressure capsule cell (HMD, Japan) and Daphne 7373 oil was used as a pressure-transmitting medium. The actual pressure in the pressure cell was determined with approximately 0.02 GPa accuracy from the linear pressure dependence of the superconducting transition of high-purity lead (dT_c/dp = 0.379 K/GPa). The residual field of the superconducting magnet was canceled before each measurement using the magnet reset option. The magnetic data for both compounds were corrected for the diamagnetic contribution as calculated with Pascal's constants. The in-phase and out-of-phase AC signal collected in the 1-500 Hz range at 25 K was subtracted from the corresponding data recorded between 2 and 14 K leading to the clean χ' and χ'' signals of the sample. Generally, the AC magnetic measurements in metallic

sample holders such as CuBe (conductors) appear to be unusable due to the significant background related to eddy currents (loops of electric current). The eddy currents lead to the in-phase and out-of-phase AC signal of the pressure cell body that are frequency dependent and much stronger than the AC magnetic susceptibility of the sample itself (Figure S32). We have noticed, however, that the AC signal of the pressure cell body is temperature independent, and used this observation to extract the magnetic signal of the sample. This works well for data up to 500 Hz, however, at frequencies >500 Hz the AC signal becomes too distorted as the eddy currents become too strong.

Computational details. Periodic DFT calculations enhanced by dispersion correction using the D3 method[68] were carried using the VASP code (version 5.4)[69-71] within the GGA approximation. The functional of Perdew,Bruke and Ernzerhof (PBE)[72] was used with a plane-wave basis set defined by an energy cut-off of 450 eV and the Projector Augmented Wave (PAW) atomic pseudopotentials.[73,74] The standard PAW potentials were used for the C, F, H, S, N and O atoms while the Dy_3 pseudopotential was used to describe the Dy atoms. The calculations were carried on the Γ-point only (adding more k-points would be too time consuming due to the large size of the unit cell). The effects of the hydrostatic pressure were enforced by the stress tensor through the PSTRESS keyword. A series of selected pressures (0, 0.12, 0.22, 0.5, 1.17, 2, 2.5, 3 and 5GPa) were used to mimic the experimental conditions and to go beyond the experimental limitations. Wavefunction-based calculations were carried out on the optimized molecular structures at every selected pressure by using the SA-CASSCF/RASSI-SO approach, as implemented in the MOLCAS quantum chemistry package (versions 8.0).[75] In this approach, the relativistic effects are treated in two steps on the basis of the Douglas–Kroll Hamiltonian. First, the scalar terms were included in the basis-set generation and were used to determine the spin-free wavefunctions and energies in the complete active space self-consistent field (CASSCF) method.[76] Next, spin-orbit coupling was added within the restricted-active-space state-interaction (RASSI-SO) method, which uses the spin-free wavefunctions as basis states.[77,78] The resulting wavefunctions and energies are used to compute the magnetic properties and g-tensors of the lowest states from the energy spectrum by using the pseudospin S = 1/2 formalism in the SINGLE_ANISO routine.[79,80] Cholesky decomposition of the bielectronic integrals was employed to save disk space and speed-up the calculations.[81] The active space of the self-consistent field (CASSCF) method consisted of the nine 4f electrons of the Dy(III) ion spanning the seven 4f orbitals, i.e. CAS(9,7)SCF. State-averaged CASSCF calculations were performed for all of the sextets (21 roots), all of the quadruplets (224 roots), and 300 out of the 490 doublets (due to software limitations) of the Dy(III) ion. 21 sextets, 128 quadruplets, and 107 doublets were mixed through spin−orbit coupling in RASSI-SO. All atoms were described by ANO-RCC basis sets.[82-84] The following contractions were used: [8s7p4d3f2g1h] for Dy atoms, [4s3p2d] for O and N atoms, [3s2p] for C atoms, [4s3p] for S atoms and [2s] for H atoms.

The dipole-dipole interaction between two magnetic centers 1 and 2, bearing the magnetic moment μ_1 and μ_2 respectively, is described as

$$H_{dip} = -\frac{1}{R_{12}^3}\,\mu_1 \cdot \mu_2 - 3(\mu_1 \cdot \vec{r}_{12})(\mu_2 \cdot \vec{r}_{12})$$

where R_{12} corresponds to the distance between the magnetic centers and $\vec{r}_{12}$ stands for the unit vector along the 12 direction. The resulting dipolar coupling J_{dip} constants were computed between the two closest Dy(III) monomers.

ASSOCIATED CONTENT

The Supporting Information is available free of charge via the Internet at http://pubs.acs.org. Magnetic, crystallographic and calculated data, Figures S1-S31 and Tables S1-S23 (PDF).

X-ray crystallographic data for **[162]Dy** at P = 0.22 GPa (CCDC 2154808), at P = 0.46 GPa (CCDC 2154806), at P = 1.17 GPa (CCDC 2154807), at P = 1.63 GPa (CCDC 2154805), at P = 2.10 GPa (CCDC 2154804) and at P = 2.43 GPa (CCDC 2154809) (CIF).

AUTHOR INFORMATION

Corresponding Author

* fabrice.pointillart@univ-rennes1.fr, boris.leguennic@univ-rennes1.fr, dawid.pinkowicz@uj.edu.pl

ORCID

Fabrice Pointillart: 0000-0001-7601-1927
Jessica Flores Gonzalez: 0000-0003-3722-8976
Charles James McMonagle: 0000-0002-5100-8913
Boris Le Guennic: 0000-0003-3013-0546
Olivier Cador: 0000-0003-2064-6223
Dawid Pinkowicz: 0000-0002-9958-3116
Michael Probert: 0000-0002-2412-7917

Author Contributions

All authors have given approval to the final version of the manuscript.

Notes

The authors declare no competing financial interest.

REFERENCES

(1)   Sessoli, R.; Tsai, H. L.; Schake, A. R.; Wang, S. Y.; Vincent, J. B.; Folting, K.; Gatteschi, D.; Christou, G.; Hendrickson, D. N. High-spin molecules: [Mn₁₂O₁₂(O₂CR)₁₆(H₂O)₄]. *J. Am. Chem. Soc.* **1993**, *115*, 1804-1816.

(2)   Sessoli, R.; Gatteschi, D.; Caneschi, A.; Novak, M. A. Magnetic bistability in a metal-ion cluster. *Nature* **1993**, *365*, 141-143.

(3)   Ishikawa, N.; Sugita, M.; Ishikawa, T.; Koshihara, S.; Kaizu, Y. Lanthanide Double-Decker Complexes Functioning as Magnets at the Single-Molecular Level. *J. Am. Chem. Soc.* **2003**, *125*, 8694-8695.

(4)   Sessoli, R.; Powell, A.K. Strategies towards single molecule magnets based on lanthanide ions. *Coord. Chem.Rev.* **2009**, *253*, 2328–2341.

(5)   Woodruff, D.N.; Winpenny, R.E.P.; Layfield, R.A. Lanthanide Single-Molecule Magnets. *Chem. Rev.* **2013**, *113*, 5110–5148.

(6)   Pointillart, F.; Cador, O.; Le Guennic, B.; Ouahab, L. Uncommon Lanthanide ions in purely 4f Single Molecule Magnets. *Coord. Chem. Rev.* **2017**, *346*, 150–175.

(7)   Zhu, Z.; Guo, M.; Li, X.-L.; Tang, J. Molecular magnetism of lanthanide: Advances and perspectives. *Coord. Chem. Rev.* **2019**, *378*, 350-364.

(8)   Gould, C. A.; McClain, K. R.; Reta, D.; Kragskow, J. G. C.; Marchiori, D. A.; Lachman, E.; Choi, E.-S.; Analytis, J. G.; Britt, R.

D.; Chilton, N. F.; Harvey, B. G.; Long, J. R. Ultrahard magnetism from mixed-valence dilanthanide complexes with metal-metal bonding, *Science* **2022**, *375*, 198-202.

(9) Chilton, N. F. Design Criteria for High-Temperature Single-Molecule Magnets. *Inorg. Chem.* **2015**, *54*, 2097-2099.

(10) Ungur, L.; Chibotaru, L. F. Ab Initio Crystal Field for Lanthanides. *Chem. Eur. J.* **2017**, *23*, 3708-3718.

(11) Guo, F.-S.; Day, B.-M.; Chen, Y.-C.; Tong, M.-L.; Mansikkamäki, A.; Layfield, R. A. A Dysprosium Metallocene Single-Molecule Magnet Functioning at the Axial Limit. *Angew. Chem., Int. Ed.*, **2017**, *56*, 11445-11449.

(12) Goodwin, C. A. P.; Ortu, F.; Reta, D.; Chilton, N. F.; Mills, D. P. Molecular magnetic hysteresis at 60 kelvin in dysprosocenium. *Nature*, **2017**, *548*, 439-442.

(13) McClain, K. R.; Gould, C. A.; Chakarawet, K.; Teat, S. J.; Groshens, T. J.; Long, J. R.; Harvey, B. G. High-temperature magnetic blocking and magneto-structural correlations in a series of dysprosium(III) metallocenium single-molecule magnets. *Chem. Sci.* **2018**, *9*, 8492-8503.

(14) Guo, F.-S.; Day, B.-M.; Chen, Y.-C.; Tong, M.-L.; Mansikkamäki, A.; Layfield, R. A. Magnetic hysteresis up to 80 kelvin in a dysprosium metallocene single-molecule magnet. *Science* **2018**, *362*, 1400-1403.

(15) Thiele, S.; Balestro, F.; Ballou, R.; Klyatskaya, S.; Ruben, M.; Wernsdorfer, W. Electrically driven nuclear spin resonance in single-molecule magnets. *Science* **2014**, *344*, 1135-1138.

(16) Pedersen, K. S.; Ariciu, A.-M.; McAdams, S.; Weihe, H.; Bendix, J.; Tuna, F.; Piligkos, S. Toward Molecular 4f Single-Ion Magnet Qubits. *J. Am. Chem. Soc.* **2016**, *138*, 5801-5804.

(17) Sato, O. Dynamic molecular crystals with switchable physical properties. *Nat. Chem.* **2016**, *8*, 644-656.

(18) Zhang, P.; Perfetti, M.; Kern, M.; Hallmen, P. P.; Ungur, L.; Lenz, S.; Ringenberg, M. R.; Frey, W.; Stoll, H.; Rauhut, G.; van Slageren, J. Exchange coupling and single molecule magnetism in redox-active tetraoxolene-bridged dilanthanide complexes. *Chem. Sci.* **2018**, *9*, 1221–1230.

(19) Dolinar, B. S.; Gomez-Coca, S.; Alexandropoulos, D. I.; Dunbar, K. R. An air stable radical-bridged dysprosium single molecule magnet and its neutral counterpart: redox switching of magnetic relaxation dynamics. *Chem. Commun.* **2017**, *53*, 2283–2286.

(20) Gonidec, M.; Davies, E. S.; McMaster, J.; Amabinino, D. B.; Veciana, J. Probing the Magnetic Properties of Three Interconvertible Redox States of a Single-Molecule Magnet with Magnetic Circular Dichroism Spectroscopy. *J. Am. Chem. Soc.* **2010**, *132*, 1756–1757.

(21) Dickie, C. M.; Laughlin, A. L.; Wofford, J. D.; Bhuvanesh, N. S.; Nippe, M. Transition metal redox switches for reversible "on/off" and "slow/fast" single-molecule magnet behavior in dysprosium and erbium bis-diamidoferrocene complexes. *Chem. Sci.* **2017**, *8*, 8039–8049.

(22) Tanaka, D.; Inose, T.; Tanaha, H.; Lee, S.; Ishikawa, N.; Ogawa, T. Proton-induced switching of the single molecule magnetic properties of a porphyrin based Tb^{III} double-decker complex. *Chem. Commun.* **2012**, *48*, 7796–7798.

(23) Liang, Z.; Damjanovic, M.; Kamila, M.; Cosquer, G.; Breedlove, B. K.; Enders, M.; Yamashita, M. Proton Control of the Lanthanoid Single-Ion Magnet Behavior of a Double-Decker Complex with an Indolenine-Substituted Annulene Ligand. *Inorg. Chem.* **2017**, *56*, 6512–6521.

(24) Suzuki, K.; Sato, R.; Mizuno, N. Reversible switching of sigle-molecule magnet behaviors by transformation of dinuclear dysprosium cores in polyoxometalates. *Chem. Sci.* **2013**, *4*, 596–600.

(25) Liu, J.-L.; Chen, Y.-C.; Zheng, Y.-Z.; Lin, W.-Q.; Ungur, L.; Wernsdorfer, W.; Chibotaru, L. F.; Tong, M.-L. Switching the

anisotropy barrier of a single-ion magnet by symmetry change from quasi-D_{5h} to quasi-O_h. *Chem. Sci.* **2013**, *4*, 3310–3316.

(26) Zhang, X.; Vieru, V.; Feng, X.; Liu, J.-L.; Zhang, Z.; Na, B.; Shi, W.; Wag, B.-W.; Powell, A. K.; Chibotaru, L. F.; Gao, S.; Cheng, P.; Long, J. R. Influence of Guest Exchange on the Magnetization Dynamics of Dilanthanide Single-Molecule-Magnet Nodes within a Metal-Organic Framework. *Angew. Chem., Int. Ed.* **2015**, *54*, 9861–9865.

(27) Ge, J.-Y.; Cui, L.; Li, J.; Yu, F.; Song, Y.; Zhang, Y.-Q.; Zuo, J.-L.; Kurmoo, M. Modulating Single-Molecule Magnetic Behavior of a Dinuclear Erbium(III) Complex by Solvent Exchange. *Inorg. Chem.* **2017**, *56*, 336–343.

(28) Pinkowicz, D.; Ren, M.; Zheng, L.-M.; Sato, S.; Hasegawa, M.; Morimoto, M.; Irie, M.; Breedlove, B. K.; Cosquer, G.; Katoh, K.; Yamashita, M. Control of the Single-Molecule Magnet Behavior of Lanthanide-Diarylethene Photochromic Assemblies by Irradiation with Light. *Chem.–Eur. J.* **2014**, *20*, 12502–11513.

(29) Wang, L.-F.; Qiu, J.-Z.; Liu, J.-L.; Chen, Y.-C.; Jia, J.-H.; Jover, J.; Ruiz, E.; Tong, M.-L. Modulation of single-molecule magnet behavior via photochemical [2+2] cycloaddition. *Chem. Commun.* **2015**, *51*, 15358–15361.

(30) Selvanathan, P.; Dorcet, V.; Roisnel, T.; Bernot, K.; Huang, G.; Le Guennic, B.; Norel, L.; Rigaut, S. *trans* to *cis* photoisomerization in merocyanine dysprosium and yttrium complexes. *Dalton Trans.* **2018**, *47*, 4139–4148.

(31) Hojorat, M.; Al Sabea, H.; Norel, L.; Bernot, K.; Roisnel, T.; Gendron, F.; Le Guennic, B.; Trzop, E.; Collet, E.; Long, J. R.; Rigaut, S. Hysteresis Photomodulation via Single-Crystal-to-Single-Crystal Isomerization of a Photochromic Chain of Dysprosium Single-Molecule Magnets. *J. Am. Chem. Soc.* **2020**, *142*, 931-936.

(32) Tian, H.; Su, J.-B.; Bao, S.-S.; Kurmoo, M.; Huang, X.-D.; Zhang, Y.-Q.; Zheng, L.-M. Reversible ON–OFF switching of single-molecule-magnetism associated with single-crystal-to-single-crystal structural transformation of a decanuclear dysprosium phosphonate. *Chem. Sci.* **2018**, *9*, 6424–6433.

(33) Pointillart, F.; Flores Gonzalez, J.; Montigaud, V.; Tesi, L.; Cherkasov, V.; Le Guennic, B.; Cador, O.; Ouahab, L.; Sessoli, R.; Kuropatov, V. Redox- and solvato-magnetic switching in a tetrathiafulvalene-based triad single-molecule magnet. *Inorg. Chem. Front.* **2020**, *7*, 2322-2334.

(34) Cador, O.; Le Guennic, B.; Pointillart, F. Electro-activity and magnetic switching in lanthanide-based single-molecule magnets. *Inorg. Chem. Front.* **2019**, *6*, 3398-3417.

(35) Suzuki, Y.; Y.; Takeda, K.; Awaga, K. Enhancement of Jahn-Teller isomerism in Mn12Ac under high quasi-hydrostatic pressure. *Phys. Rev. B* **2003**, *67*, 132402.

(36) Sieber, A.; Bircher, R.; Waldmann, O.; Carver, G.; Vhaboussant, G.; Mutka, H.; Güdel, H.-U. Effect of Pressure on the Magnetic Anisotropy in the Single-Molecule Magnet Mn12-Acetate: An Inelastic Neutron Scattering Study. *Angew. Chem., Int. Ed.* **2005**, *44*, 4239-4242.

(37) Bircher, R.; Chaboussant, G.; Dobe, C.; Güdel, H. U.; Ochsenbein, S. T.; Sieber, A.; Waldmann, O. Single-Molecule Magnets Under Pressure. *Adv. Funct. Mater.* **2006**, *16*, 209-220.

(38) Sieber, A.; Chaboussant, G.; Bircher, R.; Boskovic, C.; Güdel, H. U. Pressure dependence of the magnetic anisotropy in the single-molecule magnet Mn$_4$O$_3$Br(OAc)$_3$(dbm)$_3$. *Phys. Rev. B* **2004**, *70*, 172413.

(39) Prescimone, A.; Milios, C. J.; Moggach, S.; Warren, J. E.; Lennie, A. R.; Sanchez-Benitez, J.; Kamenev, K.; Bircher, R.; Murrie, M.; Parsons, S.; Brechin, E. K. [Mn$_6$] under Pressure: A Combined Crystallographic and Magnetic Study. *Angew. Chem., Int. Ed.* **2008**, *47*, 2828-2831.

(40) Prescimone, A.; Milios, C. J.; Sanchez-Benitez, J.; Kamenev, K. V.; Loose, C.; Kortus, J.; Moggach, S.; Murrie, M.; Warren,

J. E.; Lennie, A. R.; Parsons, S.; Brechin, E. K. High pressure induced spin changes and magneto-structural correlations in hexametallic SMMs. *Dalton Trans.* **2009**, 4858-4867.

(41)   Prescimone, A.; Sanchez-Benitez, J.; Kamenev, K. V.; Moggach, S. A.; Lennie, A. R.; Warren, J. E.; Murrie, M.; Parsons, S.; Brechin, E. K. High pressure effects on a trimetallic Mn$^{II/III}$ SMM. *Dalton Trans.* **2009**, 7390-7395.

(42)   Chen, W.-B.; Chen, Y.-C.; Liu, J.-L.; Jia, J.-H.; Wang, L.-F.; Li, Q.-W.; Tong, M.-L. A Piezochromic Dysprosium(III) Single-Molecule Magnet Based on an Aggregation-Induced-Emission-Active Tetraphenylethene Derivative Ligand. *Inorg. Chem.* **2017**, *56*, 8730-8734.

(43)   Norre, M. S.; Gao, C.; Dey, S.; Gupta, S. K.; Borah, A.; Murugavel, R.; Rajaraman, G.; Overgaard, J. High-Pressure Crystallographic and Magnetic Studies of Pseudo-D$_{5h}$ Symmetric Dy(III) and Ho(III) Single-Molecule Magnets. *Inorg. Chem.* **2020**, *59*, 717-729.

(44)   da Cunha, T. T.; Jung, J.; Boulon, M.-E.; Campo, G.; Pointillart, F.; Pereira, C. L. M.; Le Guennic, B.; Cador, O.; Bernot, K.; Pineider, F.; Golhen, S.; Ouahab, L. Magnetic Poles Determinations and Robustness of Memory Effect upon Solubilization in a Dy^{III}-Based Single Ion Magnet. *J. Am. Soc. Chem.* **2013**, *135*, 16332-16335.

(45)   Pointillart, F.; Bernot, K.; Golhen, S.; Le Guennic, B.; Guizouarn, T.; Ouahab, L.; Cador, O. Magnetic Memory in an Isotopically Enriched and Magnetically Isolated Mononuclear Dysprosium Complex. *Angew. Chem., Int. Ed.* **2015**, *54*, 1504-1507.

(46)   Tesi, L.; Salman, Z.; Cimatti, E.; Pointillart, F.; Bernot, K.; Mannini, M.; Sessoli, R. Isotope effects on the spin dynamics of single-molecule magnets probed using muon spin spectroscopy. *Chem. Commun.* **2018**, *54*, 7826-7829.

(47)   Flores Gonzalez, J.; Pointillart, F.; Cador, O. Hyperfine coupling and slow magnetic relaxation in isotopically enriched Dy^{III} mononuclear single-molecule magnets. *Inorg. Chem. Front.* **2019**, *6*, 1081-1086.

(48)   Fernandez Garcia, G.; Montigaud, V.; Norel, L.; Cador, O.; Le Guennic, B.; Totti, F.; Pointillart, F. Redox-Active Dysprosium Singe-Molecule Magnet: Spectro-Electrochemistry and Theoretical Investigations. *Magnetochemistry* **2019**, *5*, 46-60.

(49)   Llunell, M.; Casanova, D.; Cirera, J.; Alemany, P.; Alvarez, S. *SHAPE Program for the Stereochemical Analysis of Molecular Fragments by Means of Continuous Shape Measures and Associated Tools;* Departament de Quimica Fisica, Departament de Quimica Inorganica and Institut de Quimica Teorica i Computacional-Universitat de` Barcelona: Barcelona, Spain.

(50)   Pointillart, F.; Cauchy, T.; Maury, O.; Le Gal, Y.; Golhen, S.; Cador, O.; Ouahab, L. Tetrathiafulvalene-amido-2-pyridine-*N*-oxide as Efficient Charge-Transfer Antenna Ligand for the Sensitization of Yb^{III} Luminescence in a Series of Lanthanide Paramagnetic Coordination Complexes. *Chem. Eur. J.* **2010**, *16*, 11926-11941.

(51)   Abragam, A.; Bleaney, B. Electron Paramagnetic Resonance of Transition Ions, Clarendon Press, Oxford, **1970**.

(52)   Singh, A.; Shrivastava, K. N. Optical-acoustic two-phonon relaxation in spin systems, *Phys. Status Solidi B*, **1979**, *95*, 273–277.

(53)   Shrivastava, K. N. Theory of Spin-Lattice Relaxation, *Phys. Status Solidi B*, **1983**, *177*, 437–458.

(54)   Goodwin, C. A. P.; Reta, D.; Ortu, F.; Chilton, N. F.; Mills, D. P. Synthesis and Electronic Structures of Heavy Lanthanide Metallocenium Cations. *J. Am. Chem. Soc.* **2017**, *139*, 18714–18724.

(55)   Gu, L.; Wu, R. Origin of the anomalously low Raman exponents in single molecule magnets. *Phys. Rev. B* **2021**, *103*, 014401.

(56)   Orbach, R. Spin-lattice relaxation in rare-earth salts, *Proc. R. Soc. London, Ser. A*, **1961**, *264*, 458–484.

(57)   Errulat, D. Gabidullin, B.; Mansikkamaki, A.; Murugesu, M. Two Heads are Better than One: Improving Magnetic Relaxation in the Dysprosium Metallocene DyCp*$_2$BPh$_4$ Upon Dimerization by Use of an Exceptionally Weakly-Coordinating Anion. *Chem. Commun.* **2020**, *56*, 5937-5940.

(58)   Pointillart, F.; Jung, J.; Berraud-Pache, R.; Le Guennic, B.; Dorcet, V.; Golhen, S.; Cador, O.; Maury, O.; Guyot, Y.; Decurtins, S.; Liu, S.-X.; Ouahab, L. Luminescence and Single-Molecule Magnet Behavior in Lanthanide Complexes Involving a Tetrathiafulvalene-Fused Dipyridophenazine Ligand. *Inorg. Chem.* **2015**, *54*, 5384-5397

(59)   Ou-Yang, J.-K.; Saleh, N.; Fernandez Garcia, G.; Norel, L.; Pointillart, F.; Guizouarn, T.; Cador, O.; Totti, F.; Ouahab, L.; Crassous, J.; Le Guennic, B. Improved slow magnetic relaxation in optically pure helicene-based Dy^{III} single molecule magnets. *Chem. Commun.* **2016**, *52*, 14474-14477.

(60)   Lefeuvre, B.; Galangau, O.; Flores Gonzalez, J.; Montigaud, V.; Dorcet, V.; Ouahab, L.; Le Guennic, B.; Cador, O.; Pointillart, F. Field-Induced Dysprosium Single-Molecule Magnet Based on a Redox-Active Fused 1,10-Phenantroline-Tetrathiafulvalene-1,10-Phenantroline Bridging Triad. *Front. Chem.* **2018**, *6*, 552-562.

(61)   Pointillart, F.; Ou-Yang, J.-K.; Fernandez Garcia, G.; Montigaud, V.; Flores Gonzalez, J.; Marchal, R.; Favereau, L.; Totti, F.; Crassous, J.; Cador, O.; Ouahab, L.; Le Guennic, B. Tetrathiafulvalene-Based Helicene Ligand in the Design of a Dysprosium Field-Induced Single-Molecule Magnet. *Inorg. Chem.* **2019**, *58*, 52-56.

(62)   Galangau, O.; Flores Gonzalez, J.; Montigaud, V.; Dorcet, V.; Le Guennic, B.; Cador, O.; Pointillart, F. Dysprosium Single-Molecule Magnets Involving 1,10-Phenantroline-5,6-dione Ligand. *Magnetochemistry* **2020**, *6*, 19-33.

(63)   Sheldrick, G. M. Bruker Apex II; Bruker AXS Inc.: Madison, WI, **2004**.

 (64)   SAINT; Bruker AXS Inc.: Madison, WI, **2007**.

(65)   SADABS; Bruker AXS Inc., Madison, WI, **2001**.

(66)   Sheldrick, G. M. Crystal structure refinement with SHELXL. *Acta Crystallogr., Sect. C: Struct. Chem.* **2015**, *71*, 3–8.

(67)   Sheldrick, G. M. A short history of SHELX. *Acta Crystallogr., Sect. A: Found. Crystallogr.* **2008**, *64*, 112–122.

(68)   Grimme, S.; Antony, J.; Ehrlich, S.; Krieg, H. A consistent and accurate ab initio parametrization of tdensity functional dispersion correction (DFT-D) for the 94 elements H-Pu. *J. Chem. Phys.* **2010**, *132*, 154104.

(69)   Kresse, G.; Hafner, J. Ab initio molecular dynamics for liquid metals. *Phys.Rev. B* **1993**, *47*, 558-561.

(70)   Kresse, G.; Furthmüller, J. Efficiency of ab-initio total energy calculations for metals and semiconducors using plane-wave basis set. *Comput. Mat. Sci.* **1996**, 6, 15-50.

(71)   Kresse, G.; Furthmüller, J. Efficient iterative schemes for ab initio total-energy calculations using a plane-wave basis set. *Phys.Rev. B* **1996**, *54*, 11169-11186.

(72)   Perdew. J. P.; Burke. K.; Ernzerhof. M. Generalized Gradient Approximation Made Simple. *Phys. Rev. Lett.* **1996**, *77*, 3865–3868.

(73)   Blöchl, P. E. Projector augmented-wave method. *Phys. Rev. B.* **1994**, *50*, 17953-17979.

(74)   Kresse, G.; Joubert, D. From ultrasoft pseudopotentials to the projector augmented-wave method. *Phys.Rev. B.* **1999**, *59*, 1758-1775.

(75)   Aquilante. F.; Autschbach. J.; Carlson. R. K.; Chibotaru. L. F.; Delcey. M. G.; De Vico. L.; Galván. I. F.; Ferré. N.; Frutos. L. M.; Gagliardi. L.; Garavelli. M.; Giussani. A.; Hoyer. C. E.; Manni. G. L.; Lischka. H.; Ma. D. X.; Malmqvist. P.; Müller. T.; Nenov. A.; Olivucci. M.; Pedersen. T. B.; Peng. D. L. ; Plasser. F.; Pritchard. B.; Reiher. M. ; Rivalta. I.; Schapiro. I.; Segarra-Martí. J.; Stenrup. M.; Truhlar. D. G. ; Ungur. L.; Valentini. A.; Vancoillie. S.;

Veryazov. V.; Vysotskiy. V. P.; Weingart. O.; Zapata. F.; Lindh. R. Molcas 8: New Capabilities for Multiconfigurational Quantum Chemical Calculations Across the Periodic Table. *J. Comput. Chem.* **2016**, *37*, 506–541.

(76)   Roos. B. O.; Taylor. P. R.; Siegbahn. P. E. M. A complete active space SCF method (CASSCF) using a density matrix formulated super-CI approach. *Chem. Phys.* **1980**, *48*, 157-288.

(77)   Malmqvist. P. A.; Roos. B. O.; Schimmelpfennig. B. The restricted active space (RAS) state interaction approach with spin-orbit coupling. *Chem. Phys. Lett.* **2002**, *357*, 230–240.

(78)   Malmqvist. P. A.; Roos. B. O. The CASSCF state interaction method. *Chem. Phys. Lett*. **1989**, *155*, 189–194.

(79)   Chibotaru. L. F.; Ungur. L. Ab initio calculation of anisotropic magnetic properties of complexes. I. Unique definition of pseudospin Hamiltonians and their derivation. *J. Chem. Phys.* **2012**, *137*, 064112–064122.

(80)   Chibotaru. L. F.; Ungur. L.; Soncini. A. The Origin of Nonmagnetic Kramers Doublets in the Ground State of Dysprosium Triangles: Evidence for a Toroidal Magnetic Moment. *Angew. Chem., Int. Ed.* **2008**, *47*, 4126–4129.

(81)   Aquilante. F.; Malmqvist. P.-A.; Pedersen. T.-B.; Ghosh. A.; Roos. B. O. Cholesky Decomposition-Based Multiconfiguration Second-Order Perturbation Theory (CD-CASPT2): Application to the Spin-State Energetics of CoIII(diiminato)(NPh). *J. Chem. Theory Comput.* **2008**, *4*, 694–702.

(82)   Roos. B. O.; Lindh. R.; Malmqvist. P.-A.; Veryazov. V.; Widmark. P.-O. Main Group Atoms and Dimers Studied with a New Relativistic ANO Basis Set. *J. Phys. Chem. A* **2004**, *108*, 2851–2858.

(83)   Roos. B. O.; Lindh. R.; Malmqvist. P.-A.; Veryazov. V.; Widmark. P.-O. New Relativistic ANO Basis Sets for Transition Metal Atoms. *J. Phys. Chem. A* **2005**, *109*, 6575–6579.

(84)   Roos. B. O.; Lindh. R.; Malmqvist. P.-A.; Veryazov. V.; Widmark. P.-O.; Borin. A.-C. New relavistic Atomic Natural Orbital Basis Sets for lanthanide Atoms with Applications to the Ce Diatom and LuF3. *J. Phys. Chem. A* **2008**, *112*, 11431–11435.